Dielectric barrier discharge in air with a controllable spatial distribution : a tomographic investigation

Dielectric barrier discharge in air with a controllable spatial distribution—a tomographic investigation

2016 J. Phys. D: Appl. Phys. 49 195204

(http://iopscience.iop.org/0022-3727/49/19/195204)

IOP Publishing Journal of Physics D: Applied Physics
J. Phys. D: Appl. Phys. **49** (2016) 195204 (7pp) doi:10.1088/0022-3727/49/19/195204

Dielectric barrier discharge in air with a controllable spatial distribution—a tomographic investigation

M van der Schans, A Sobota and G M W Kroesen

Department of Applied Physics, Eindhoven University of Technology, PO Box 513, 5600 MB Eindhoven, The Netherlands

E-mail: m.van.der.schans@tue.nl

Received 13 January 2016, revised 8 March 2016
Accepted for publication 21 March 2016
Published 14 April 2016

Abstract

A novel dielectric barrier discharge source with a controllable discharge distribution has been designed for operation in atmospheric air. A predictable distribution has been achieved through the design of the powered electrode and the dielectric barrier. Optical emission tomography is used to study the discharge distribution. The method and its applicability in studies of non-symmetric plasmas are discussed in the paper. The results show that a desired discharge distribution may be achieved through the manipulation of the electric field amplification by the powered electrode and it is found that the discharge shape resembles the field imposed at the powered electrode only. Together with the flexibility of the plasma source design, this can prove highly advantageous for the treatment of irregularly shaped surfaces in plasma medicine and plasma surface processing at atmospheric pressure.

Keywords: dielectric barrier discharge, air plasma, optical emission tomography, mesh electrode

(Some figures may appear in colour only in the online journal)

1. Introduction

Dielectric barrier discharges (DBDs) are a class of plasma sources that consist of a discharge gap with one or multiple dielectrics and produce non-thermal plasma at atmospheric pressure [1, 2]. The combined advantages of non-thermal atmospheric pressure plasma and scalability has led to many industrial applications of DBDs, including ozone production, surface modification, excimer lamps and plasma displays [1, 3].

Recently, biomedical applications of non-thermal plasmas, such as tissue sterilization and regeneration, wound healing and treatment of skin diseases, have received much interest [4–7]. One potential plasma source for these applications is a DBD, operated in open air while using the treatment target as one of the electrodes [8, 9]. However, since tissue and wounds generally do not constitute a flat surface, a non-rigid DBD source that accommodates to irregularly shaped surfaces and produces a controllable discharge distribution is desirable, in order to ensure a controllable coverage of the treated target.

A controllable discharge distribution is not inherently present in atmospheric pressure DBDs due to the fact that the dynamics of the transient discharge are for a large part governed by the charge deposited on the dielectric barrier in a single voltage cycle or pulse [1, 3, 10]. Although diffuse and patterned DBDs at atmospheric pressure have been reported in literature, streamer breakdown in atmospheric pressure air DBDs generally results in filaments randomly distributed over the surface of the DBD [1, 3, 11].

In order to tame the random distribution inherent in atmospheric air DBDs, the powered electrode of the new plasma source presented in this paper is given a mesh structure, which in combination with a thin dielectric barrier results in local electric field amplification in the discharge gap. From the fact that the discharge forms at spots of highest electric field, the amplification is used as a means to control the discharge distribution. In several previous studies [12–15], it was already shown that metal wire meshes (usually attached to a larger rigid electrode), can be used to increase the uniformity of a

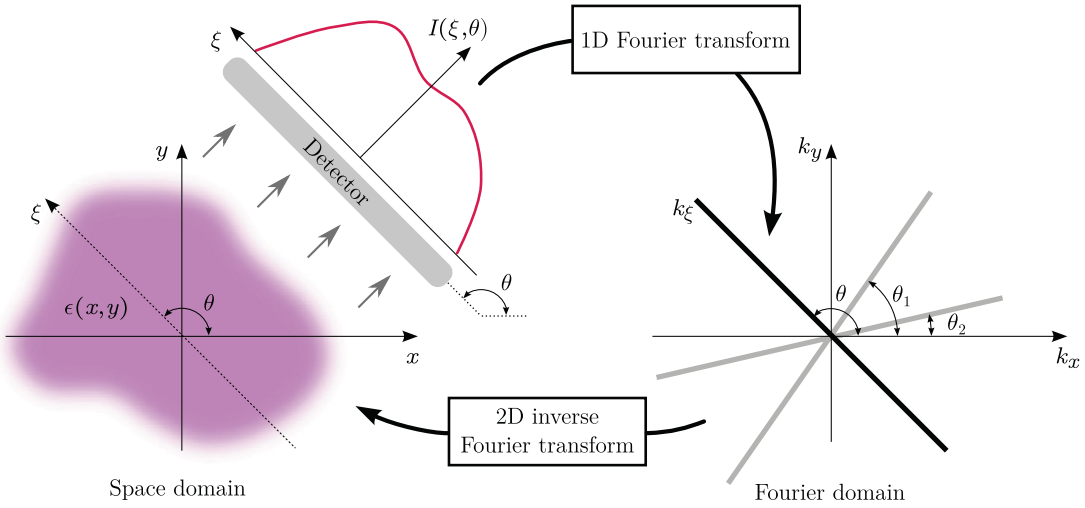

Figure 1. The concept of radon inversion: the local emission coefficient $\epsilon(x, y)$ of an irregularly shaped region of plasma (purple) is integrated along a lateral set of lines of sight by the detector, which makes an angle θ with the x-axis. A slice of the 2D Fourier spectrum at the same angle θ is acquired by 1D Fourier transforming the measured intensity profile. Slices at different angles are used to assemble the 2D Fourier spectrum, which after an 2D inverse Fourier transform results in $\epsilon(x, y)$. In practice however, with only a finite number of slices, the 2D inverse Fourier transform step is realized by a reconstruction algorithm.

DBD. Additionally, in this work flexible and thin materials are used in the construction of the powered electrode and dielectric barrier in order to produce a non-rigid DBD source that works in air at atmospheric pressure.

To investigate the spatial distribution of the discharge resulting from a geometry with a mesh electrode, optical emission tomography is applied. This technique allows full spatial reconstruction of the local emission from multiple light intensity measurements of the discharge, even when the discharge distribution has no symmetry at all. Probably best known for its application in medical imaging, tomography uses information obtained from multiple different viewing angles. It has been used before in plasma research in the analysis of several types of discharge lamps [16–18], low pressure inductively coupled plasmas [19, 20], thermal arc discharges [21], as well as in flame diagnostics [22]. Its application to the emission of a DBD has however not yet been reported in literature.

In this paper it is shown that it is possible to form a DBD discharge in air with a controllable distribution. The area that the discharge in this work covers measures roughly 30 mm^2. The proof of a controllable structure on this scale is given by means of optical emission tomography. The implications on the role of surface and volume charges in maintaining this DBD structure are discussed at the end of the paper.

2. Optical emission tomography

This section outlines the principles of tomography applied to optical emission in 2D using filtered back-projection relevant for this work. More details on the mathematics of tomography and generalizations to higher dimensions can be found in [23, 24].

For an optically thin plasma, in which absorption is assumed negligible, the observed light intensity I (W m^{-2} sr^{-1}) is a line-integrated quantity $I = \int_L \epsilon(\boldsymbol{r})\,\mathrm{d}r$, where $\epsilon(\boldsymbol{r})$ (W m^{-3} sr^{-1}) is the local emission coefficient and L is a path describing the line of sight along which the light is observed [25].

While the integrated line intensity is the variable that can be measured, for the analysis of the spatial structure and properties of the plasma the local emission coefficient is required. If the plasma is axially or spherically symmetric, and hence $\epsilon = \epsilon(r)$, the widely used Abel inversion method can be applied [25]. However, if the plasma exhibits a more complex symmetry or no symmetry at all, the more general method of radon inversion has to be applied. Many different tomographic reconstruction algorithms that enact radon inversion exist, but the transform-based filtered back-projection (FBP) method is most popularly used [24]. FBP requires access to ample viewing angles and a high signal-to-noise ratio (SNR) in the intensity measurements at individual angles. In cases where the number of viewing angles is limited, by for example the windows of a vessel, or where a sufficiently high SNR cannot be obtained, specialized reconstruction methods using regularization theory are generally applied. Examples of such methods include the maximum entropy method [26–29] and the recently published method based on the minimization of a Mumford–Shah type functional [30]. In the present case however, operation of the discharge in open air allows in principle an arbitrary number of viewing angles and a sufficiently high SNR in the individual measurements is expected to successfully use FBP for reconstruction.

The concept of radon inversion—obtaining the local emission coefficient $\epsilon(x, y)$ from a set of intensity profiles $I(\xi, \theta)$ taken at different angles θ—is illustrated in figure 1. As shown on the right side (Fourier domain side) of figure 1, a slice of the 2D Fourier spectrum of $\epsilon(x, y)$ at angle θ with the k_x-axis is obtained by Fourier transforming an intensity measurement at angle θ with the x-axis. Repeating this process, the 2D Fourier spectrum of $\epsilon(x, y)$ can be assembled from intensity measurements at different angles. Finally, an inverse 2D Fourier transform yields $\epsilon(x, y)$ and finishes the radon inversion.

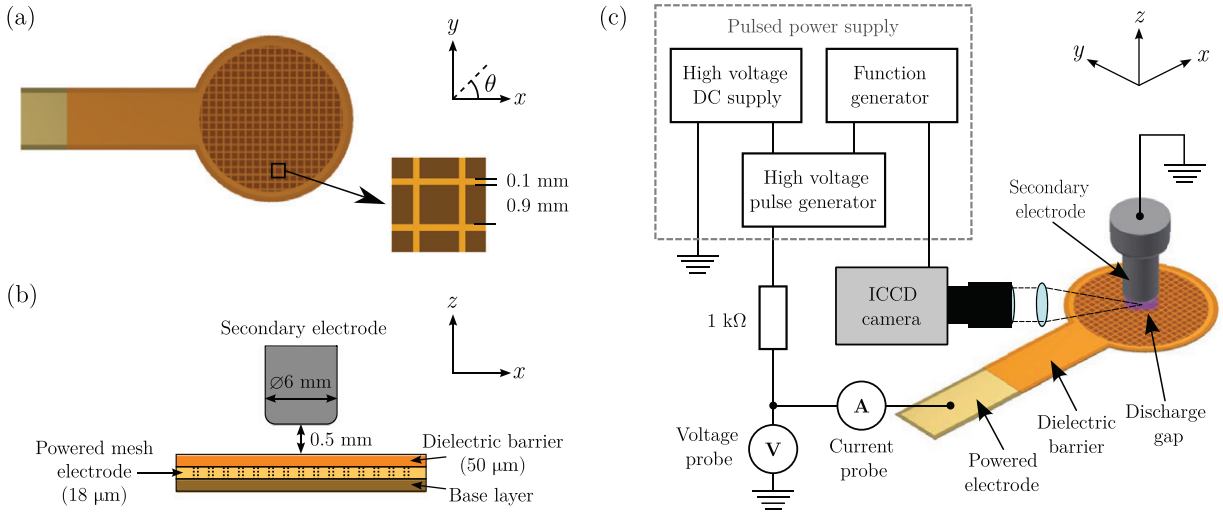

Figure 2. Schematic drawings of the experimental setup. In (a) a detailed view of the meshed electrode is given and (b) illustrates the discharge geometry. A schematic overview of the electronics used to operate the plasma source is shown in (c). The plasma in the discharge gap in (c) is illustrated in purple.

In practice however, only a finite number of slices are used and the 2D inverse Fourier transform cannot be applied directly to the entire Fourier spectrum. Instead, filtered back-projection can be applied slice by slice for a set of slices that is uniformly distributed over 180° [24]. *Back-projection* is a name for the dual radon transform common in the context of image processing. The general form of the filtered back-projection is

$$\begin{aligned} Q(\xi,\theta) &= \frac{1}{4\pi^2}\int_{-\infty}^{\infty}\hat{I}(k_\xi,\theta)\,\mathrm{e}^{\mathrm{i}k_\xi\xi}|k_\xi|\,\mathrm{d}k_\xi \\ &= \frac{1}{2\pi}\mathcal{F}_1^{-1}\left[\hat{I}(k_\xi,\theta)\,|k_\xi|\right] \\ &= \frac{1}{2\pi}\mathcal{F}_1^{-1}\left[\mathcal{F}_1[I(\xi,\theta)]\,|k_\xi|\right]. \end{aligned} \tag{1}$$

As can be seen from (1) the filtered projection $Q(\xi,\theta)$ is, apart from a constant $(2\pi)^{-1}$, the projection $I(\xi,\theta)$ multiplied by a linear ramp filter $|k_\xi|$ in frequency space. This filter emphasizes the higher frequencies relative to the lower frequencies. Proper implementation of this filter thus demands a high SNR in the $I(\xi,\theta)$ measurements. Mathematically, the ramp filter is a natural result of the coordinate transformation $(k_x,k_y)\rightarrow(k_\xi,\theta)$, but its necessity can also be understood intuitively from the right side of figure 1: with a finite amount of slices there is more information on the lower frequencies compared to the higher frequencies. Sometimes the filter $|k_\xi|$ is multiplied by an additional window function to de-emphasize or cut the highest frequencies and eliminate noise effects. However, in this case care should be taken not to cut the highest frequencies of the actual signal, which would result in a blurred reconstructed image.

The local emission coefficient that is needed for the analysis of the spatial structure and properties of the discharge is given by

$$\epsilon(x,y) = \int_0^{\pi} Q(\xi,\theta)\,\mathrm{d}\theta. \tag{2}$$

Together (1) and (2) constitute the FBP algorithm: $Q(\xi,\theta)$ is calculated for all viewing angles θ using (1), and then according to (2), $\epsilon(x,y)$ is obtained by summing all the individual $Q(\xi,\theta)$. Note that in the back-projection operation every point along the same line of sight gets the same contribution from the corresponding individual $Q(\xi,\theta)$.

3. Experimental setup

A schematic drawing of the setup is shown in figure 2. The powered electrode is a 18 μm thick conductive NiAu-plated copper layer printed on top of a polyimide base layer. In the circular area the conductive layer has a square mesh structure (0.1 mm thick conductive channels along a 1 mm × 1 mm square grid), as illustrated in figure 2(a), which is covered by a 50 μm thick polyimide layer that functions as dielectric barrier. A grounded cylindrical stainless steel electrode with a diameter of 6 mm is placed 0.5 mm above the polyimide barrier to create the discharge gap, as shown in figure 2(b).

Positive unipolar high voltage (HV) pulses with a pulse width of 1 μs, a repetition rate of 1 kHz and a pulse height of 6 kV are used to drive the discharge. These particular parameters are chosen because they result in an average discharge distribution that is reproducible for at least the time it takes to record all the intensity profiles required for tomographic reconstruction. While a discharge is ignited already at a pulse height of 4.3 kV, it is not stable from cycle to cycle until nearing 6 kV. On the other hand, when the voltage is further increased above approximately 7 kV, increasingly more intense surface discharges on the dielectric barrier rapidly degrade the polyimide material and changes in the discharge are visibly observed.

A total overview of the electronics and imaging system is shown in figure 2(c). The pulsed power supply consists of an HV pulse generator (DEI PVX-4110) that uses a pulse shaped signal from a function generator (Agilent 3320A) to

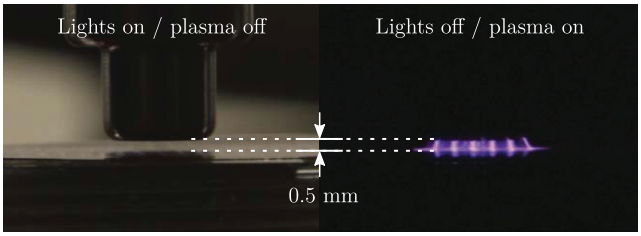

Figure 3. Photographs (made with a DSLR camera) of the discharge geometry with the lights on and the power supply off (left) and the visual appearance of the discharge with the lights off and the power supply on (right). The surface of the polyimide barrier is reflective and therefore some reflections are visible in the bottom parts of the photographs.

gate the voltage of an HV DC supply (Spellman UHR10P60). The output of the pulsed power supply is connected to the exposed part of the NiAu-plated copper electrode through a 1 kΩ resistor.

Photographs (made with a DSLR camera) of the discharge gap and the resulting discharge as it appears to the eye, viewed along one direction of the mesh channels, are shown in the left and right parts of figure 3 respectively.

For the tomographic reconstruction an intensified charge coupled device (ICCD) camera (Stanford Computer Optics 4Picos) is used to record the light emitted by the discharge. A UV camera lens (CoastalOpt UV-Micro-Apo) and an additional quartz lens are used to image the discharge gap onto the CCD. In this optical system the 0.5 mm gap between the dielectric barrier and grounded electrode is imaged onto 17 vertical pixels. The camera is externally triggered by the same function generator as the HV pulse generator, while the delay and gate time are controlled through the camera's software. The discharge cell as a whole is mounted to a rotation stage in order to record the intensity from different angles. The orientation of the powered electrode is illustrated in figure 2(a), where θ has the same definition as in figure 1.

Finally, an HV probe (Tektronix P6015A) is placed parallel to the discharge cell to measure the applied voltage and a current probe (Pearson 6585) is placed in series with the discharge cell at the HV side to measure the current. The voltage and current signals are shown in figure 4. By multiplying the voltage and current signals and integrating over the cycle period the energy dissipation per cycle can be calculated [31]. Under the present experimental conditions an average energy dissipation of 0.13 ± 0.01 mJ per cycle is found, which at a repetition rate of 1 kHz corresponds to an average power of 0.13 ± 0.01 W.

Besides displacement current, there are two discharge current peaks visible in the bottom part of figure 4, one on the rising edge and the other on the falling edge of the voltage pulse. In this work only the discharge on the rising edge pulse is investigated using emission tomography. The gate time of the ICCD camera is indicated by the gray area in figure 4. Since the discharge on the rising edge of the pulse has a temporal jitter of approximately 10 ns, the gate time of the ICCD is set to 100 ns to ensure all emitted light during each individual discharge is recorded. Furthermore, as barrier discharges in air are typically filamentary, the emission

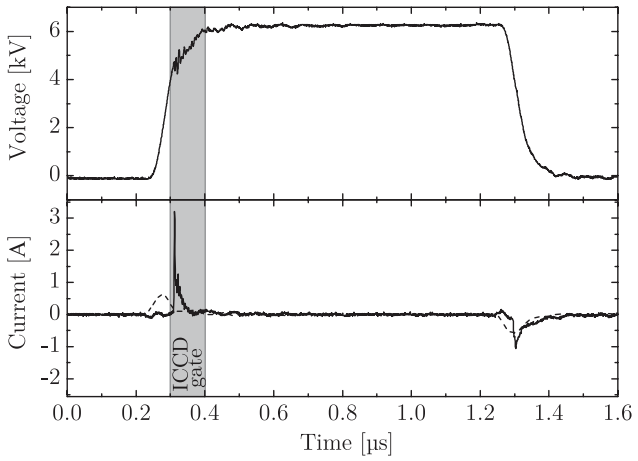

Figure 4. Voltage (top) and current (bottom) signals measured by their corresponding probe. In the bottom graph the discharge current (solid line) and displacement current (dashed line) are shown individually. The gate time of the ICCD camera is indicated by the gray area.

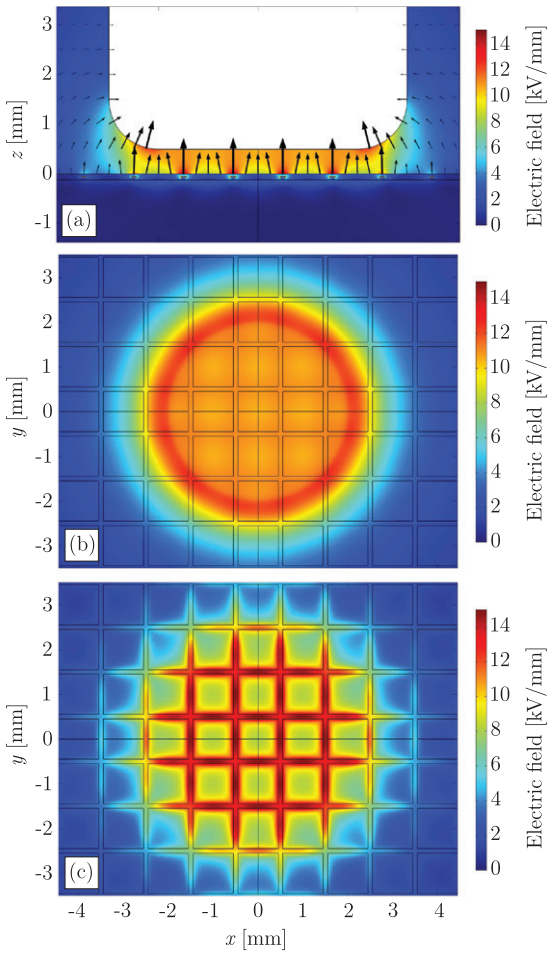

Figure 5. Cross sections of the field strength from the electrostatic model: (a) a vertical cross section ($y = 0$ plane), (b) a horizontal cross section just below the grounded electrode ($z = 0.499$ mm plane), and (c) a horizontal cross section just above the barrier ($z = 0.001$ mm plane). The white area in figure (a) indicates the grounded electrode, and an overlay of black lines indicating the location of the mesh is shown in figures (b) and (c).

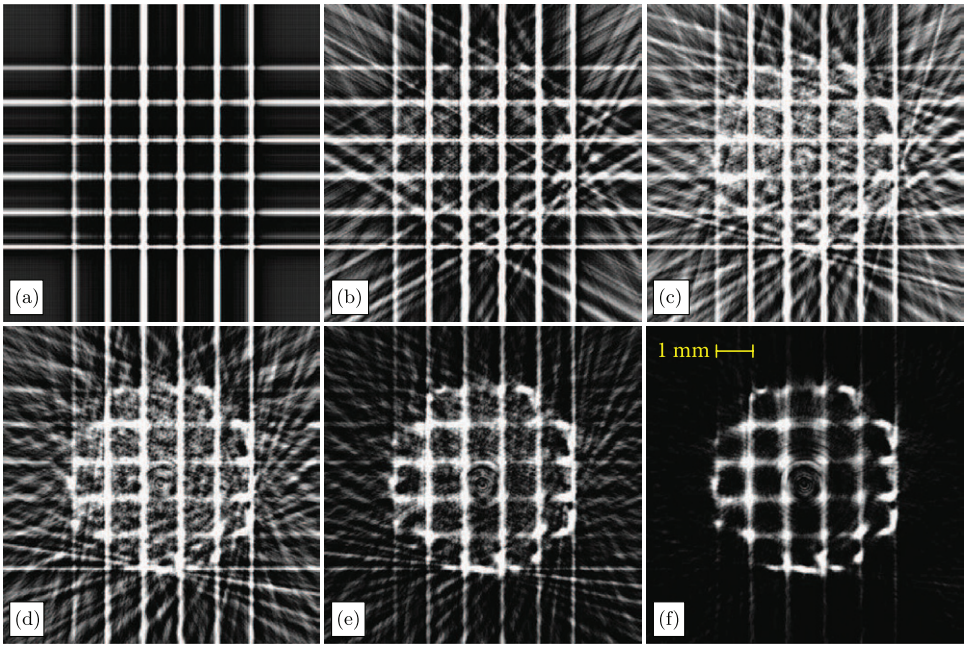

Figure 6. Reconstructed local emission in the $z = 0.25$ mm plane using (a) 2 angles, (b) 6 angles, (c) 12 angles, (d) 20 angles, (e) 30 angles and (f) 60 angles. Each of the images shows approximately 9 mm × 9 mm.

of 500 discharges is accumulated into a single intensity measurement for each angle to obtain the average intensity distribution.

To study the field amplification effects of the mesh structured electrode an electrostatic model of the discharge geometry is constructed using COMSOL®. While an electrostatic model does not result in any information on the discharge itself, it does provide qualitative information on the electric field distribution in the gap before the discharge. Since the discharge geometry has no axial symmetry, a 3D model has been used. In the calculations the top surface of the barrier is placed in the $z = 0$ plane and a voltage of 6 kV is assigned to the powered electrode.

Figure 5 shows three cross sections of the calculated electric field strength. In the vertical cross section in figure 5(a) two sources of field amplification can be observed, one resulting from the curvature of the grounded electrode and other from the sharp features of the mesh electrode. The amplification by the grounded electrode results in a circular pattern in the field strength just below grounded electrode, as shown in figure 5(b), and the amplification by the mesh results in a mesh pattern in the field strength right above the dielectric, as shown in figure 5(c).

4. Results and discussion of the method

The discharge at the rise of the voltage pulse is recorded with the ICCD camera, as described in section 3, at 60 angles ranging from $\theta = 0°$ to $\theta = 177°$ with an interval of $\Delta\theta = 3°$. The angle $\theta = 0°$ is chosen such that its corresponding lines of sight are parallel to one direction of the grid of the mesh electrode (see figure 2(a)). Before discussing the reconstructed local emission resulting from applying FBP to these measurements, the required SNR and number of angles used in the reconstruction for this geometry are considered.

Firstly an estimation of the average SNR in the measurements will be given, as this is an important property connected to the applicability of the tomographic method. The average SNR can be calculated by $\mathrm{SNR} = \mu_{\mathrm{ROI}}/\sigma_{\mathrm{BG}}$, where μ_{ROI} is the average intensity in the region of interest (ROI), here chosen as $(-3.5\ \mathrm{mm} < \xi < 3.5\ \mathrm{mm})$ and $(0 < z < 0.5\ \mathrm{mm})$, and σ_{BG} the standard deviation of the background (BG), outside the ROI. Averaged over the measurements at all 60 angles this gives $\mathrm{SNR} = 149$. It is empirically found in this study that under the present conditions this value is sufficiently high to use the ramp filter in (1) without the need for an additional window function to cut the highest frequencies.

Besides a sufficiently high SNR, a sufficient number of angles is required for FBP to obtain an accurate reconstruction and to minimize aliasing artifacts [24]. To investigate the effects of the number of angles used in the reconstruction of the present geometry, the local emission in the middle of the gap ($z = 0.25$ mm) is reconstructed using different subsets of the in total 60 measurements. The results are shown in figure 6. When only two angles are used (figure 6(a)), the reconstructed image consists of two sets of parallel streaks, one of which corresponds to the peaks in the 0° projection and the other to a similar profile measured at 90°. Adding more angles to the reconstruction reproduces the distribution of light emission in the middle of the reconstructed image. While the qualitative distribution of the local emission becomes apparent from 20 angles (figure 6(d)) onwards, the streak artifacts outside the circular region containing the discharge only decrease to a relative level that is significantly below the actual emission for 60 angles (figure 6(f)).

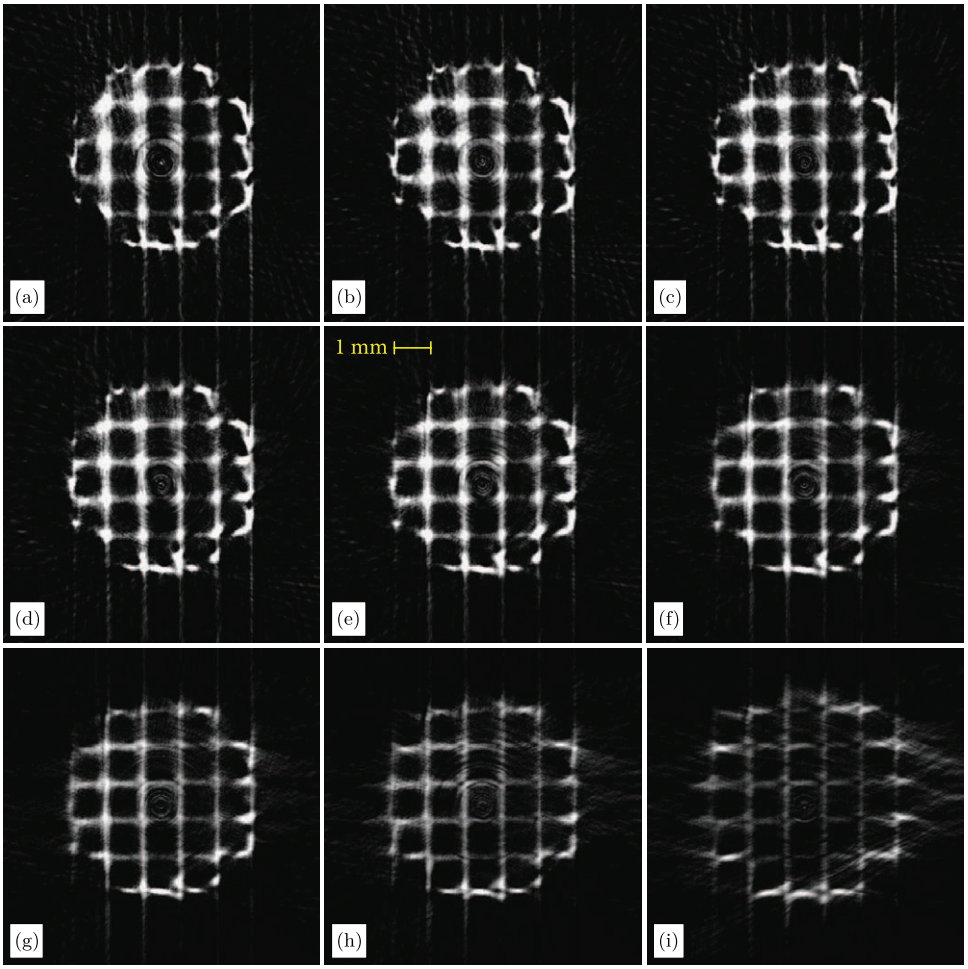

Figure 7. Reconstructed cross sections of the local emission using 60 angles for (a) $z = 0.50$ mm—the grounded electrode, (b) $z = 0.44$ mm, (c) $z = 0.38$ mm, (d) $z = 0.31$ mm, (e) $z = 0.25$ mm, (f) $z = 0.19$ mm, (g) $z = 0.13$ mm, (h) $z = 0.06$ mm and (i) $z = 0$ mm—the powered meshed electrode. Each of the images shows approximately 9 mm × 9 mm.

5. Analysis of the spatial structure of the discharge

Nine cross sections of the reconstructed local emission at different positions in the gap using the measurements at all 60 angles are presented in figure 7. The figure shows that the discharge distribution throughout the gap resembles the pattern of the powered electrode and is governed by its shape. This indicates that the discharge distribution may be controlled through the design of the powered electrode.

Comparing the results in figure 7 to the static electric field simulations shown in figure 5 points towards the electric field profile imposed by the meshed electrode as one of the responsible mechanisms for the observed discharge distribution. Increasing the thickness of the barrier would therefore cause the loss of structure, as was verified in experiments, where a barrier thickness of 500 μm was sufficient to cause the loss of meshed discharge structure and instead a random distribution of filaments was observed.

It is assumed that the behavior of the discharge as well as its spatial distribution is governed by an additional effect—the 'memory effect'—where the charge left over from the previous discharge is dense enough to locally serve as an electron source for subsequent discharges. The fact that the discharge structure is well defined at the grounded electrode ($z = 0.50$ mm), which itself has no pattern nor a dielectric barrier for charges to collect on, suggests that volume charges left over from the previous discharge play an important role. Indeed, while the memory effect of DBDs is often attributed to surface charge deposited on the barrier during the preceding discharge, Akishev *et al* proposed that spatial memory is actually due to residual plasma density in the volume [32], which acts as pre-ionization for the next discharge, and is present still in air at low driving frequencies. Xu *et al* also found through numerical calculations that the structure and pattern formation in a glow DBD is dependent on the distribution of volume charges rather than on surface charges [33]. This is further supported by experimental investigations into the influence of volume memory effects in a pulsed-driven single filament DBD in a N_2/O_2 mixture (0.1 vol% O_2) performed by Kettlitz *et al* [34] and Höft *et al* [35]. By varying the duty cycle (and thereby changing the time between discharges) they found differences in breakdown behavior that are correlated to a change in volume pre-ionization.

On the other end of the discharge gap at the surface of the barrier ($z = 0$ mm), the discharge can be seen spreading outwards along the structure of the mesh electrode outside the diameter of the grounded electrode of 6 mm. This shows that the deposited surface charges cause large enough electric

fields along the dielectric surface to cause surface discharges spreading outwards along the meshed structure. Increasing the pulse voltage results in visibly more intense and extended surface discharges along the meshed structure. This is in accordance with the fact that pulsed driven DBDs have been shown to transfer a large amount of charge compared to sinusoidally driven DBDs [36] and that the transferred charge increases with pulse voltage [34].

6. Conclusions and outlook

In this work the application of tomography using filtered back-projection to a unipolar positively pulsed dielectric barrier discharge with a mesh electrode in open air is presented. It is demonstrated that by accumulating the light emitted by the discharge at the rising edge for 500 cycles at 60 individual angles results in a sufficiently high signal-to-noise ratio and number of viewing angles for a 3D reconstruction of the average local emission in this discharge geometry.

The paper demonstrates the possibility for obtaining a DBD in air at atmospheric pressure that has a controllable structure, which is not a property of a typical air DBD. The discharge has been shown to have a similar structure in the entire discharge gap. This property shows that it is both possible to design the structure of the discharge by designing the powered electrode and to retain this distribution on the grounded electrode or another surface when considering applications. Together with the flexibility that is achieved with a mesh electrode covered by a thin dielectric, this may be highly advantageous for the treatment of irregularly shaped surfaces in plasma medicine and plasma surface processing at atmospheric pressure.

For future investigations into the presented discharge a barrier material that is more resilient to plasma exposure will be implemented in the source, which should allow for a more detailed parameter study. While investigating the discharge dynamics on sub-nanosecond timescales is currently not feasible using tomographic measurements, varying repetition frequency and duty cycle, as well as recording images for the discharge on the falling edge of the pulse may further elucidate the role of volume memory and pre-ionization in governing the discharge structure throughout the discharge gap.

References

[1] Kogelschatz U 2003 *Plasma Chem. Plasma Process.* **23** 1–46
[2] Fridman A, Chirokov A and Gutsol A 2005 *J. Phys. D: Appl. Phys.* **38** R1–24
[3] Kogelschatz U 2002 *IEEE Trans. Plasma Sci.* **30** 1400–8
[4] Kong M G, Kroesen G, Morfill G, Nosenko T, Shimizu T, van Dijk J and Zimmermann J L 2009 *New J. Phys.* **11** 115012
[5] Fridman G, Friedman G, Gutsol A, Shekhter A B, Vasilets V N and Fridman A 2008 *Plasma Process. Polym.* **5** 503–33
[6] Laroussi M 2009 *IEEE Trans. Plasma Sci.* **37** 714–25
[7] von Woedtke T, Reuter S, Masur K and Weltmann K D 2013 *Phys. Rep.* **530** 291–320
[8] Fridman G, Peddinghaus M, Balasubramanian M, Ayan H, Fridman A, Gutsol A and Brooks A 2006 *Plasma Chem. Plasma Process.* **26** 425–42
[9] Fridman G, Shereshevsky A, Jost M M, Brooks A D, Fridman A, Gutsol A, Vasilets V and Friedman G 2007 *Plasma Chem. Plasma Process.* **27** 163–76
[10] Becker K H, Kogelschatz U, Schoenbach K H and Barker R J (ed) 2005 *Non-Equilibrium Air Plasmas at Atmospheric Pressure* (*Series in Plasma Physics*) (Bristol: Institute of Physics Publishing)
[11] Bogaczyk M, Nemschokmichal S, Wild R, Stollenwerk L, Brandenburg R, Meichsner J and Wagner H E 2012 *Contrib. Plasma Phys.* **52** 847–55
[12] Okazaki S, Kogoma M, Uehara M and Kimura Y 1993 *J. Phys. D: Appl. Phys.* **26** 889–92
[13] Wang X, Luo H, Liang Z, Mao T and Ma R 2006 *Plasma Sources Sci. Technol.* **15** 845–8
[14] Fang Z, Qiu Y, Zhang C and Kuffel E 2007 *J. Phys. D: Appl. Phys.* **40** 1401–7
[15] Ye Q, Wu Y, Li X, Chen T and Shao G 2012 *Plasma Sources Sci. Technol.* **21** 065008
[16] Denisova N, Revalde G, Skudra A and Bogans E 2006 *J. Phys. D: Appl. Phys.* **39** 1069–77
[17] Denisova N, Haverlag M, Ridderhof E J, Nimalasuriya T and van der Mullen J J A M 2008 *J. Phys. D: Appl. Phys.* **41** 144021
[18] Denisova N, Gavare Z, Revalde G, Skudra J and Veilande R 2011 *J. Phys. D: Appl. Phys.* **44** 155201
[19] Okigawa A, Tadokoro M, Itoh A, Nakano N, Petrović Z L and Makabe T 1997 *Japan. J. Appl. Phys.* **36** 4605–16
[20] Miyoshi Y, Petrović Z L and Makabe T 2002 *IEEE Trans. Plasma Sci.* **30** 130–1
[21] Franceries X, Freton P, Gonzalez J J, Lago F and Masquère M 2005 *J. Phys. D: Appl. Phys.* **38** 3870–84
[22] Denisova N, Tretyakov P and Tupikin A 2013 *Combust. Flame* **160** 577–88
[23] Deans S R 1983 *The Radon Transform and Some of its Applications* (Chichester: Wiley)
[24] Kak A C and Slaney M 2001 *Principles of Computerized Tomographic Imaging* (*Classics in Applied Mathematics*) (Philadelphia: SIAM)
[25] Kunze H J 2009 *Introduction to Plasma Spectroscopy* (*Springer Series on Atomic, Optical, and Plasma Physics*) (Berlin: Springer)
[26] Gull S and Daniell G 1978 *Nature* **272** 686–90
[27] Gull S F and Newton T J 1986 *Appl. Opt.* **25** 156
[28] Denisova N V 1999 *J. Phys. D: Appl. Phys.* **31** 1888–95
[29] Denisova N 2009 *IEEE Trans. Plasma Sci.* **37** 502–12
[30] Facchi P, Ligabò M and Solimini S 2015 *Phys. Scr.* **90** 074007
[31] Pipa A V, Koskulics J, Brandenburg R and Hoder T 2012 *Rev. Sci. Instrum.* **83** 115112
[32] Akishev Y, Aponin G, Balakirev A, Grushin M, Karalnik V, Petryakov A and Trushkin N 2011 *Plasma Sources Sci. Technol.* **20** 024005
[33] Xu S W, He F, Wang Y, Li L and Ouyang J T 2013 *Phys. Plasmas* **20** 083515
[34] Kettlitz M, Höft H, Hoder T, Reuter S, Weltmann K D and Brandenburg R 2012 *J. Phys. D: Appl. Phys.* **45** 245201
[35] Höft H, Kettlitz M, Becker M M, Hoder T, Loffhagen D, Brandenburg R and Weltmann K D 2014 *J. Phys. D: Appl. Phys.* **47** 465206
[36] Kettlitz M, Höft H, Hoder T, Weltmann K D and Brandenburg R 2013 *Plasma Sources Sci. Technol.* **22** 025003